



Nanoscale

Epitaxial Stabilization versus Interdiffusion: Synthetic Routes to Metastable Cubic HfO₂ and HfV₂O₇ from the Core–Shell Arrangement of Precursors

Journal:	<i>Nanoscale</i>
Manuscript ID	NR-ART-08-2019-007316.R1
Article Type:	Paper
Date Submitted by the Author:	23-Oct-2019
Complete List of Authors:	Fleer, Nathan; Texas A&M University, Department of Chemistry Thomas, Melonie; University of Kentucky Andrews, Justin; Texas A&M University, Department of Chemistry Waetzig, Gregory; Texas A&M University, Department of Chemistry Gonzalez, Oscar; Texas A&M University, Department of Chemistry Liu, Guan-Wen; Texas A&M University, Department of Chemistry Guiton, Beth; University of Kentucky, ; Oak Ridge National Laboratory, Banerjee, Sarbajit; Texas A&M University, Department of Chemistry

SCHOLARONE™
Manuscripts

ARTICLE

Epitaxial Stabilization versus Interdiffusion: Synthetic Routes to Metastable Cubic HfO₂ and HfV₂O₇ from the Core–Shell Arrangement of Precursors

Received 00th January 20xx,
Accepted 00th January 20xx

DOI: 10.1039/x0xx00000x

Nathan A. Fleeer,^{a,b} Melonie P. Thomas,^c Justin L. Andrews,^{a,b} Gregory R. Waetzig,^{a,b} Oscar Gonzalez,^a Guan-Wen Liu,^{a,b} Beth S. Guiton,^{c*} and Sarbajit Banerjee^{a,b*}

Metastable materials that represent excursions from thermodynamic minima are characterized by distinctive structural motifs and electronic structure, which frequently underpins new function. The binary oxides of hafnium present a rich diversity of crystal structures and are of considerable technological importance given their high dielectric constants, refractory characteristics, radiation hardness, and anion conductivity; however, high-symmetry tetragonal and cubic polymorphs of HfO₂ are accessible only at substantially elevated temperatures (1720 and 2600°C, respectively). Here, we demonstrate that the core–shell arrangement of VO₂ and amorphous HfO₂ promotes outwards oxygen diffusion along an electropositivity gradient and yields an epitaxially matched V₂O₅/HfO₂ interface that allows for the unprecedented stabilization of the metastable cubic polymorph of HfO₂ under ambient conditions. Free-standing cubic HfO₂, otherwise accessible only above 2600°C, is stabilized by acid etching of the vanadium oxide core. In contrast, interdiffusion under oxidative conditions yields the negative thermal expansion material HfV₂O₇. Variable temperature powder X-ray diffraction demonstrate that the prepared HfV₂O₇ exhibits pronounced negative thermal expansion in the temperature range between 150 and 700°C. The results demonstrate the potential of using epitaxial crystallographic relationships to facilitate preferential nucleation of otherwise inaccessible metastable compounds.

Introduction

Metastable crystal structures with atomic connectivities somewhat altered from the thermodynamic phase correspond to relatively shallower local minima on free energy landscapes but can in many instances be trapped under ambient conditions.^{1–4} The large amounts of energy inputted in conventional high-temperature ceramic and metallurgical processing methods result in reaction mixtures being able to efficiently approach equilibrium. In contrast, synthetic approaches that can situate the material in a local minimum under specific constraints (temperature, pressure, voltage, strain, chemical doping) can often be rapidly “quenched”, enabling kinetic trapping of metastable atomic configurations.^{3,5–11} Perhaps the most iconic example of a metastable material that can be isolated under ambient conditions is diamond, which exhibits a distinctly different bonding motif, and thus vastly different functionality, as compared to its thermodynamically stable counterpart, graphite.^{12,13} Seminal work by Garvie several decades ago established synthetic routes to the stabilization of the metastable tetragonal polymorph of ZrO₂.¹⁴ At nanoscale dimensions, the increased stabilization of the tetragonal polymorph derived from surface and strain energy differentials with the monoclinic polymorph overcomes the bulk free

energy preference for the latter polymorph.^{5,15} The transformation of metastable tetragonal ZrO₂ to the thermodynamically stable monoclinic polymorph provides an effective means of energy dissipation and is used industrially for transformation toughening.^{15–20} Recent work illustrates that the stabilization of tetragonal HfO₂ under ambient conditions is much more challenging and requires scaling to dimensions <4 nm as compared to the ca. 30 nm critical size for ZrO₂.^{5,15,20} In this work, we describe a synthetic strategy for stabilizing the energetically still more disfavored cubic phase of HfO₂ under ambient conditions, which as per the binary Hf–O phase diagram is stable only above 2600°C.²¹

The binary phase diagram of Hf–O reported by Shin et al. delineates cubic HfO₂ as a relatively small sliver stable only for oxygen stoichiometries between 0.5 and 0.7 mole fraction in the temperature range between 2600 and 2758°C.²¹ Here we show that a combination of epitaxial growth of HfO₂ onto VO₂ nanocrystals and interdiffusion, followed by etching of the vanadium oxide core enables the stabilization of metastable cubic HfO₂ under ambient conditions. In contrast, annealing core–shell VO₂@HfO₂ nanocrystals under oxidative conditions promotes effective interdiffusion, stabilizing the negative thermal expansion material, HfV₂O₇.

HfO₂ and ZrO₂ are commonly referred to as the “twin oxides” owing to the similarities in the properties of these two materials that arises from the closely matched atomic radii of their cations, which indeed is a direct result of lanthanide contraction.^{22–24} Under ambient conditions, hafnia crystallizes in a low-symmetry (seven-coordinated hafnium atoms) monoclinic phase (M, space group *P*₂₁/*c*) and

^a Department of Chemistry, Texas A&M University, 3255 TAMU, 580 Ross St, College Station, Texas 77843, USA.

^b Department of Materials Science and Engineering, Texas A&M University, 575 Ross St, College Station, Texas 77843, USA.

^c Department of Chemistry, University of Kentucky, 505 Rose Street, Lexington, Kentucky 40506, USA

exhibits a diffusionless Martensitic transition to a higher-symmetry (with eight-coordinated hafnium atoms) tetragonal structure (R, space group $P4_2/nmc$) at a temperature of ca. 1720°C.^{5,15} An even higher symmetry (still with eight-coordinated hafnium atoms) cubic phase (C, space group $Fm\bar{3}m$) is stabilized at temperatures above 2600°C and is retained until hafnia is congruently melted at a temperature of 2758°C.^{5,25–27} Traversing the free energy landscape along the pressure axis reveals two oxygen-deficient orthorhombic variants, orthorhombic I (O1, space group $Pca2_1$), which is stabilized above 4.3 GPa and orthorhombic II (O2, space group $Pmn2_1$), which is observed above 14.5 GPa.^{26,28} The dielectric constant of monoclinic HfO₂ is in the vicinity of 18, substantially higher than that of SiO₂, whereas tetragonal and cubic polymorphs are predicted to have dielectric constants approaching 70 and 30, respectively.^{5,15,24}

By reacting HfCl₄ with hafnium(IV) *tert*-butoxide (Hf(O^tBu)₄) with the addition of low concentrations of the less reactive cerium(IV) *tert*-butoxide and lanthanum(III) isopropoxide, we have recently separated nucleation and growth steps, enabling the stabilization of HfO₂ nanocrystals with dimensions <10 nm.¹⁵ The development of this synthetic route reveals the critical threshold for stabilizing tetragonal HfO₂ as being 3.6–3.8 nm.¹⁵ Another approach to stabilization of tetragonal HfO₂ involves the introduction of multiple nanotwinned domains within the monoclinic variant; the twin planes serve to nucleate the transformation dislocation and mediate stabilization of the tetragonal phase at temperatures more than 1000°C lower than the bulk transformation temperature.^{5,29} While these efforts have enabled stabilization of the technologically important tetragonal polymorph of HfO₂, the higher temperature cubic phase remains difficult to access. Aliovalent doping has been utilized to stabilize cubic HfO₂ but requires dopant concentrations as high as 11.0 and 3.00 at.% for V and La, respectively. Intriguingly, lanthanum-doped cubic HfO₂ exhibits a remarkably high dielectric constant of 38.^{30,31} While dimensional confinement and twin domain control have emerged as viable means of accessing the tetragonal phase of HfO₂, an altogether new strategy is required to stabilize the cubic polymorph of HfO₂ and is demonstrated here based on a core–shell precursor strategy. The intimate mixing and small diffusion lengths within core-shell VO₂@HfO₂ nanocrystals enables the facile stabilization of phase-pure cubic HfO₂ at low temperatures. In contrast, facilitating interdiffusion under oxidative conditions yields HfV₂O₇, a negative thermal expansion (NTE) material in the MX₂O₇ material family that exhibits isotropic negative thermal expansion.^{32–35} The development of a facile synthetic route to this material further mitigates a major impediment to its industrial use within zero thermal expansion composites.

Experimental

Synthesis of VO₂ Nanocrystals: VO₂ nanowires with lateral dimensions of 180±70 nm and lengths of 1.6±0.9 μm have been prepared by the hydrothermal reduction of V₂O₅ with acetone as reported in previous work.^{36–38} Briefly, 1.60 mg V₂O₅, 42.0 mL acetone, and 33.0 mL of deionized water ($\rho=18.2$ MΩ·cm, Barnstead Water Purification System) were placed in a 125 mL polytetrafluoroethylene vessel, which in turn was placed within a sealed hydrothermal reactor and maintained at 210°C for 72 h.^{36–38} The recovered solid was filtered and washed three times with water and subsequently three times with acetone. The recovered powder was then dried and annealed within a tube furnace under a flow of Ar gas (50 sccm); the furnace was heated to 550°C at a heating rate of ca. 43°C/min and held at this temperature for 5 h. The annealed solid, VO₂ nanowires crystallized in the M1 phase, was then removed and used as prepared in further reactions.

Quasi-spherical VO₂ nanocrystals with a diameter of 44±30 nm have been prepared by an alternative sol–gel condensation and hydrothermal treatment route.^{36,37,39,40} Briefly, VO(OH)₂ was precipitated from the reaction between NH₄VO₃ and N₂H₄ in deionized water at a temperature of 80°C. The solid precipitate was then heated at 210°C for 24 h within the hydrothermal apparatus described above. The recovered powder was washed with copious amounts of water and acetone across three cycles of resuspension and centrifugation.

Deposition of HfO₂ onto VO₂ Nanocrystals: Amorphous HfO₂ shells were deposited onto nanowires and quasi-spherical nanocrystals of VO₂ through a hydrolysis approach analogous to the Stöber method for the preparation of SiO₂ shells.^{36,37,46,47} In the first step, 30 mg of nanowires or quasi-spherical nanocrystals of VO₂ crystallized in the M1 phase were dispersed in 80 mL dry ethanol (dried over molecular sieves with 4 Å pore size and Na₂SO₄) *via* ultrasonication (Branson 5510) for ca. 10 min. The colloidal dispersion was then placed within a three-neck round-bottomed flask, which was attached to an Ar Schlenk line and cooled using an ice bath. Hf(O^tBu)₄ was added dropwise to the ethanol dispersion at a molar ratio of VO₂:Hf(O^tBu)₄ of 1:0.5 under an Ar ambient; the reaction mixture was then allowed to stir for 20 min. This dispersion was then removed from the ice bath, placed on a heating mantle, and heated to 80°C while maintaining an Ar ambient. Next, 20 mL of a 1:20 (v/v) H₂O:EtOH mixture was added dropwise to initiate hydrolysis of the hafnium alkoxide. The low water content precludes homogeneous nucleation of HfO₂ nanocrystals in solution and constrains HfO₂ deposition to the surfaces of the VO₂ nanocrystals. The reaction mixture was maintained at 80°C for 15 min and subsequently removed from heat and allowed to cool to ca. 50°C before moving to centrifugation. The solid precipitate was then recovered by centrifugation at 8700 rpm using a Heraeus Megafuge 8. The recovered solid was resuspended in ethanol and recovered by centrifugation at 8700 rpm. Two such cycles were performed. Dry samples were annealed in a quartz tube placed within a tube furnace under 50 sccm of flowing Ar at 650°C for 25 min. The annealed powder was then allowed to cool to room temperature before further analysis.

Stabilization of Cubic HfO₂ by Dissolution of the V₂O₃ core of V₂O₃@HfO₂ Core–shell Nanocrystals: After annealing to obtain V₂O₃@HfO₂ core–shell nanocrystals, the vanadium oxide shell was etched in acid solution to stabilize cubic HfO₂. Specifically, V₂O₃@HfO₂ core–shell nanocrystals were placed in a 5.67 M aqueous solution of HCl at a concentration of 1 mg solid per mL of solution. The prepared dispersion had a pH <1, which results in the dissolution of V₂O₃ and remnant VO₂ from the core.⁴¹ The acid-treated sample was sonicated vigorously for ca. 1 h to ensure dissolution of the core. The supernatant turned light blue in color indicating the stabilization of vanadium oxide clusters.⁴⁸ The solid was then recovered by centrifugation at 8700 rpm. The recovered solid was subsequently redispersed in ethanol and collected by centrifugation at 8700 rpm two times before being allowed to dry at room temperature.

Synthesis of HfV₂O₇: VO₂@HfO₂ core–shell nanocrystals were prepared as discussed above and the recovered powders were placed in a quartz tube and annealed under a static air ambient within a tube furnace ramping at a rate of 20°C/min to 650°C. The furnace was maintained at 650°C for 25 min. The recovered solid was light orange in appearance and was analyzed upon cooling to room temperature.

Characterization: Low-magnification transmission electron microscopy (TEM) images were recorded on a JEOL JEM-2010

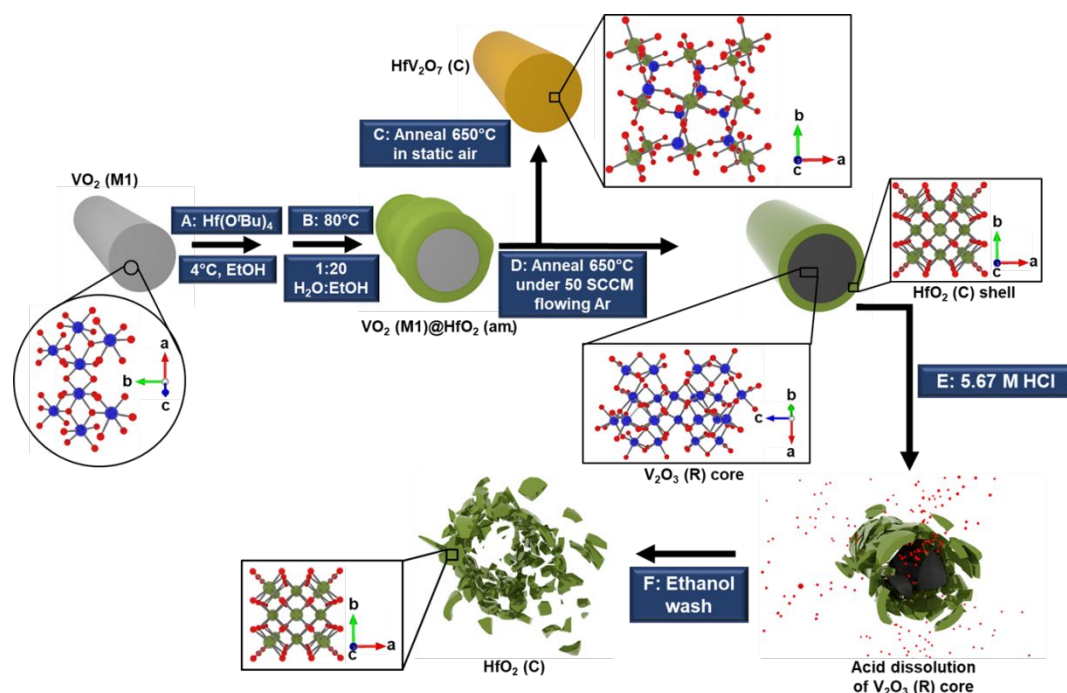


Figure 1: Schematic depiction of the synthesis of cubic HfO_2 and HfV_2O_7 from VO_2 and HfO_2 precursors arranged in a core–shell arrangement. A) $\text{Hf}(\text{O}^i\text{Bu})_4$ is deposited onto the surface of VO_2 nanowires and nanocrystals crystallized in the M1 phase and hydrolyzed in B) to deposit an amorphous HfO_2 shell. The VO_2 @amorphous- HfO_2 core–shell structures can either be C) annealed under static air at 650°C to yield cubic HfV_2O_7 , or D) annealed under flowing Ar to produce rhombohedral V_2O_3 with a cubic HfO_2 shell. E) Acid treatment of V_2O_3 @ HfO_2 with a 5.67M aqueous solution of HCl results in the dissolution of the V_2O_3 core and after F) washing with ethanol yields phase-pure cubic HfO_2 , which is recovered upon centrifugation.

instrument operated with an accelerating voltage of 200 kV. Atomic-resolution TEM images were recorded on an FEI Tecnai G2 F20 ST FE-TEM at Texas A&M University and a Nion UltraSTEM 200 microscope at Oak Ridge National Laboratory. Samples were dropcast onto copper grids after dispersion in hexanes (e-chips in the case of the Nion UltraSTEM). Both instruments were operated at an accelerating voltage of 200 kV. Scanning electron microscopy (SEM) images were recorded on a JEOL JSM-7500F field-emission scanning electron microscope set at an accelerating voltage of 10 kV.

In-situ powder X-ray diffraction (XRD) experiments were performed using a Bruker D8-Vario X-ray powder diffractometer using a $\text{Cu K}\alpha$ ($\lambda=1.5418\text{\AA}$) source operated at a 40 kV accelerating voltage with a 40 mA current. An MTC oven attachment was used for the heating experiments, which were performed under a flowing N_2 (40 sccm) environment, with patterns recorded at 50°C intervals. Refinements of powder XRD patterns were performed for patterns recorded using a Bruker D8 Advance Eco X-Ray powder diffractometer with a $\text{Cu K}\alpha$ ($\lambda=1.5418\text{\AA}$) source scanning at $1.9^\circ/\text{min}$.

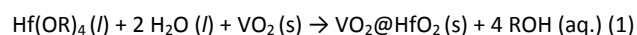
Fourier transform infrared (FTIR) data was acquired using a Bruker VERTEX-70 FTIR instrument equipped with a PIKE MIRacle single-reflection horizontal attenuated total reflectance (ATR) accessory. Neutron Activation Analysis (NAA) was performed using the Texas Engineering and Experiment Station 1-MW TRIGA reactor. Neutron irradiations of 30 s were performed at a thermal neutron fluence rate of $9.1\times 10^{12}\text{ cm}^{-2}\cdot\text{s}^{-1}$. γ -ray spectra were obtained using an HPGe detector for 500 s after a 270 s decay interval. Data analyses were performed using software from Canberra Industries.

Results and Discussion

Stabilizing Metastable Cubic HfO_2 :

VO_2 nanowires with lateral dimensions of $180\pm 70\text{ nm}$ and lengths of $1.6\pm 0.9\text{ }\mu\text{m}$ have been prepared by the acetone reduction of V_2O_5 under hydrothermal conditions as discussed in detail in the Methods section.^{36–38} Quasi-spherical VO_2 nanocrystals with diameters of $44\pm 30\text{ nm}$ have been prepared by sol–gel reduction–condensation of NH_4VO_3 with hydrazine followed by hydrothermal treatment, also as discussed in the Methods section.^{36,37,39,40} Figures S1A and B (Supporting Information) show representative transmission electron microscopy (TEM) images of the as-prepared VO_2 nanowires and quasi-spherical nanocrystals, respectively. Figure S1C plots their corresponding powder X-ray diffraction (XRD) patterns, attesting to the crystallization of both the nanowires and the nanocrystals in the monoclinic M1 phase. Pronounced Scherrer broadening is observed in the XRD pattern acquired for ultrasmall VO_2 nanocrystals owing to their small X-ray coherent domain sizes.

The synthetic approach to core–shell positioning of the precursors and the process used to prepare metastable cubic HfO_2 and the negative thermal expansion material, HfV_2O_7 is illustrated in **Figure 1**. An amorphous HfO_2 shell is first deposited onto VO_2 nanocrystals or VO_2 nanowires by hydrolysis and condensation of a hafnium alkoxide precursor as per:



This reaction is performed at low temperature (4°C) to prevent homogeneous nucleation of HfO_2 nanocrystals. The abundant hydroxyl groups on the surfaces of the VO_2 nanocrystals allow for formation of V–O–Hf oxo linkages as observed previously in the deposition of SiO_2 shells.^{36,37}

Powder XRD patterns acquired along the synthetic scheme sketched in Figure 1 are shown in Figure S2 providing evidence for the phase

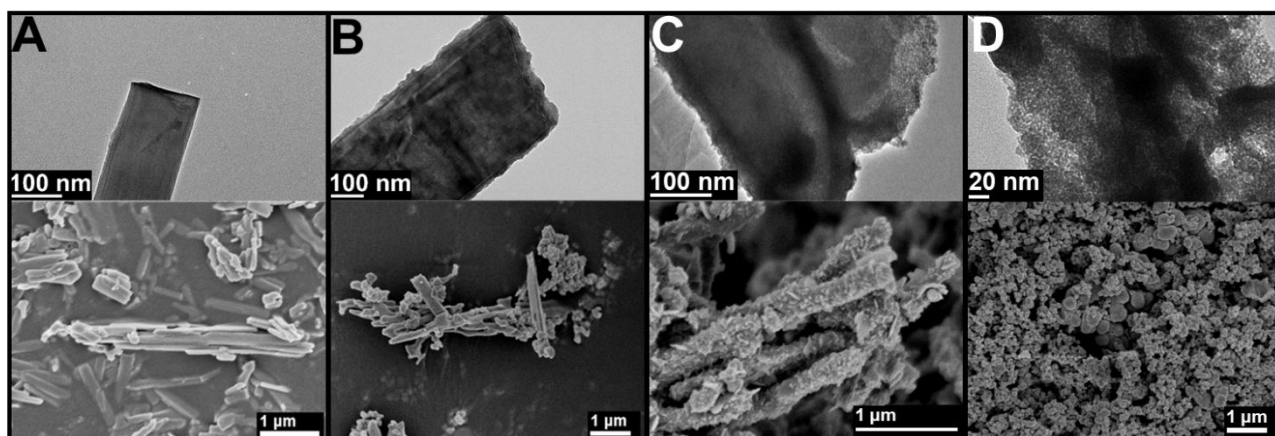
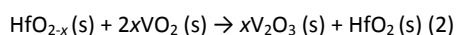


Figure 2: TEM and SEM images corresponding to synthetic steps involved in the stabilization of cubic HfO₂. **A)** TEM image (top) and SEM image (bottom) of M1-phase VO₂ nanowires prepared by the hydrothermal reduction of V₂O₅ by acetone. **B)** TEM and SEM images of VO₂ nanowires coated with an amorphous HfO₂ shell. **C)** TEM and SEM images of V₂O₃@cubic-HfO₂ core—shell structures obtained upon annealing VO₂@amorphous-HfO₂ structures at 650°C. **D)** TEM and SEM image of polycrystalline cubic HfO₂ after acid etching of the V₂O₃ core.

assignments. Figure S2B shows the appearance of a diffuse scattering background upon deposition of an amorphous HfO₂ shell onto the VO₂ nanowires. Such a diffuse scattering background suggests an amorphous shell. Annealing in Ar to 650°C results in the emergence of rhombohedral V₂O₃ (PDF: 85-1411) and crystalline cubic HfO₂ phases (Fig. S2C), illustrating oxygen diffusion from the core to the shell concomitant with crystallization consistent with the more electropositive nature of hafnium:



Based on first principles calculations, the average oxygen vacancy formation energy in amorphous HfO₂ is 6.97 eV, but is notably increased to 7.29 eV in crystalline HfO₂.^{49,50} In other words, crystallization is accompanied by a significant destabilization of oxygen vacancies, which are healed by diffusing oxygen from the VO₂ core to the HfO₂ shell. As such, crystallization of the HfO₂ shell is accompanied by a reduction in the concentration of oxygen vacancies and concomitant reduction of the vanadium(IV) oxide to vanadium(III) oxide. Acid etching of the core—shell structure leaves behind cubic HfO₂ as the only crystalline phase (Fig. S2D). No HfV₂O₇ contamination is observed for materials obtained by this method.³¹ **Figure S3** shows powder XRD patterns acquired along the same sequence of reactions for quasi-spherical VO₂ nanocrystals.

The core-shell disposition of the oxide precursors, the establishment of a crystallographically related interface between rhombohedral V₂O₃ and cubic HfO₂, and etching of the vanadium oxide core to yield freestanding cubic HfO₂ has further been examined using electron microscopy and energy dispersive X-ray spectroscopy. **Figures 2A** and **B** shows TEM and scanning electron microscopy (SEM) images of bare VO₂ nanowires and the nanowires encased by an amorphous HfO₂ shell, respectively. **Figure 2C** shows the nanowires after annealing under Ar at 650°C for 25 min; oxygen diffusion from the core to the shell results in reduction of M1 VO₂ to rhombohedral V₂O₃ and yields V₂O₃@HfO₂ core—shell particles with a cubic HfO₂ shell. The SEM image in **Figure 2C** reveals that the shell is polycrystalline with faceted plate-like crystallites protruding from the surface of the nanowires. **Figure 2D** shows cubic HfO₂ nanocrystals after acid etching of the rhombohedral V₂O₃ core. **Figure S4** (Supporting Information) shows analogous images across the sequence of reactions for quasi-spherical VO₂ nanocrystals.

Additional evidence for the core-shell configuration comes from examination of microtomed nanowires. **Figures 3A** and **B** show low-magnification TEM images of core—shell V₂O₃@HfO₂ nanowires obtained upon annealing alongside an energy-dispersive X-ray spectroscopy (EDX) map illustrating the core—shell arrangement of the vanadium and hafnium oxide domains. **Figure 3A** shows a panoramic view, whereas **Figure 3B** exhibits a cross-sectional image and EDX map acquired for an ultramicrotomed nanowire. This image shows that vanadium (red) is concentrated within the core of the structure, whereas hafnium (green) is concentrated within the shell. Further evidence of the core—shell structure comes from **Figure S5**, which shows a cross-sectional view of an ultramicrotomed nanowire as well as an EDX line scan that further confirms the core—shell structure with Hf concentrated within the shell and vanadium within the core. Some V content is detected within the shell likely derived from the outwards diffusion of vanadium cations facilitated by the miscibility of the two cations.³¹ The lattice-resolved HRTEM images in **Figures 3C** and **D** demonstrate the epitaxial matching between the rhombohedral V₂O₃ core and cubic HfO₂ shell. The direction of epitaxy in the interfacing phase is further indicated in **Figure S6 a-d**. **Figures S6 e** and **f** show the parallel green-dashed arrows along (-111) diffraction spots of cubic HfO₂ and (-1-10) diffraction spots of rhombohedral V₂O₃, which confirms the epitaxy between two phases. **Figures 3D** and **E** delineate lattice spacings of 2.95 ± 0.08 Å corresponding to the separation between (111) planes of cubic-HfO₂ and 2.68 ± 0.07 Å corresponding to the separation between (1-20) planes of rhombohedral V₂O₃. Indeed, this epitaxial matching is critical to the nucleation of cubic HfO₂.

The dynamical evolution of VO₂ nanoparticles coated with amorphous HfO₂ shells upon thermal annealing has been examined by *in situ* powder X-ray diffraction and transmission electron microscopy. **Figure 4A** plots intensity modulation maps illustrating the evolution of the powder XRD patterns of VO₂@amorphous HfO₂ core—shell structures as a function of temperature upon annealing under a N₂ ambient. Reflections corresponding to the M1 phase of VO₂ disappear at ca. 590–600°C and reflections that can be indexed to cubic HfO₂ emerge in the temperature range of 560–675°C. The crystallization and reduction of VO₂ to V₂O₃ occurs in concert and involves oxygen diffusion along a gradient of electropositivity. As noted above, oxygen vacancies are strongly destabilized as a result

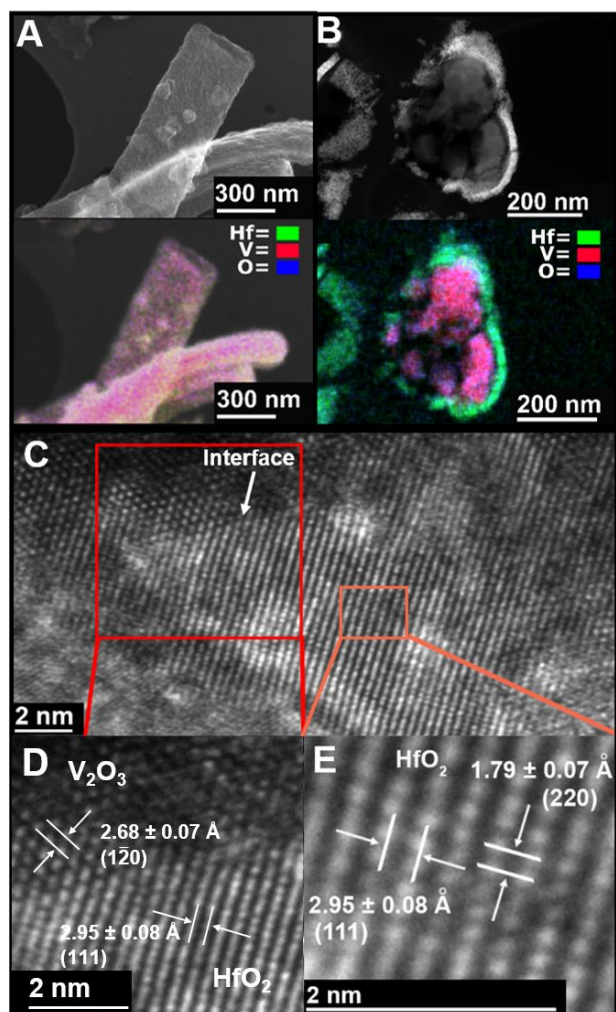


Figure 3: Imaging and compositional mapping of $V_2O_3@HfO_2$ core-shell structures. **A)** TEM image of annealed $V_2O_3@HfO_2$ and corresponding EDX map illustrating the vanadium oxide core surrounded by a hafnium oxide shell. **B)** Cross-sectional TEM image and EDX map of an ultramicrotomed core-shell nanowire. It is apparent that V (red) is highly concentrated within the core, whereas the Hf signal (green) is concentrated along the shell. **C, D)** High-resolution TEM images depicting the epitaxial interface between rhombohedral V_2O_3 and cubic HfO_2 . Lattice spacings corresponding to rhombohedral V_2O_3 (PDF 85-1411) and cubic HfO_2 are delineated. **E)** A magnified image of cubic HfO_2 domains within the shell.

of crystallization and thus oxygen atoms diffuse from the vanadium oxide core to incipient crystalline HfO_2 domains resulting in a decrease in the formal valence of vanadium within the core.^{49,50} Figure 4B shows the results of an identical reaction performed without the presence of VO_2 . Initially nucleated cubic/tetragonal domains are lost and the thermodynamically stable monoclinic phase of HfO_2 is stabilized as a result of grain growth.^{5,15–17,25} The epitaxial relationship between V_2O_3 and cubic HfO_2 in the crystalline core-shell structures is therefore critical to preventing reversion to the thermodynamically stable monoclinic polymorph at elevated temperatures. **Figure 5** shows high-resolution TEM images along with corresponding selected area electron diffraction patterns acquired upon *in situ* annealing of core-shell configurations of VO_2

nanocrystals with an amorphous HfO_2 shell. The initially amorphous HfO_2 domains are transformed to cubic HfO_2 at ca. 560°C and such domains persist upon heating up to 700°C. Cubic HfO_2 and rhombohedral V_2O_3 domains are clearly discernible upon annealing to 560°C. **Figure 5** shows the crystallite size of cubic- HfO_2 is 8.4 ± 1.4 nm.

HfO_2 exhibits high stability in aqueous media across a wide pH range; in contrast, V_2O_3 is readily dissolved in acidic media.⁴¹ This difference in reactivity provides a means of isolating free-standing cubic HfO_2 powders. The V_2O_3 cores of $V_2O_3@HfO_2$ core-shell structures have been etched in acid solution at room temperature, thereby preserving the metastable cubic structure of the shell. Refinement of the powder XRD pattern provides corroboration of the cubic crystal structure, which crystallizes in the $Fm\bar{3}m$ space group with a lattice constant of $a = 5.04793(22)\text{\AA}$ (Figure 4D and Table S1). Figure 4C shows a lattice-resolved image of free-standing cubic HfO_2 particles (prepared by acid etching of core-shell $V_2O_3@HfO_2$) acquired along the [110] zone axis. Based on analysis of the powder XRD pattern and lattice-resolved TEM images, the recovered materials are phase pure. **Figure S7** shows an O-H stretching peak at 3315 cm^{-1} in a FTIR spectrum acquired for the acid-etched sample indicating the presence of Hf-OH species after aqueous acid treatment.

Neutron activation analysis (NAA) quantification of the recovered solids reveals a V concentration of ca. 7.18 ± 0.17 at.%, likely derived from the diffusion of vanadium atoms from within the core given the reasonable solubility of vanadium within the hafnia lattice. Notably, vanadium incorporation alone cannot account for stabilization of the metastable cubic polymorph; previous studies have indicated the need for at least 11 at.% V dopant incorporation to stabilize cubic HfO_2 , which is observed to further be contaminated by HfV_2O_7 .^{31,42}

The stabilization of cubic HfO_2 stems from both kinetic origins as well as from the conditions of constrained equilibrium imposed by the small crystallite size.^{1,3,4} The change in free energy accompanying a transition from a thermodynamically stable (TS) to metastable (MS) phase can be described by the following expression:

$$\Delta G_{TS-MS} = G_{TS}^c - G_{MS}^c + U_{TS} - U_{MS} + S_{TS} - S_{MS} \dots (3)$$

where G^c , U , and S denote the chemical free energy (dependent on temperature owing to entropic contributions), strain energy, and surface energy, respectively; the subscripts TS and MS denote the thermodynamic and metastable polymorphs, respectively.^{3,4,51} Monoclinic HfO_2 is the thermodynamically stable phase and thus ΔG^c is a large positive number on the order of several hundred meV.^{3,4,51} In order for cubic HfO_2 to emerge as the thermodynamically stable species, the strain and surface energy terms have to strongly favor stabilization of the cubic polymorph. Recent calculations suggest that surface facets of cubic HfO_2 can indeed be substantially lower in energy;⁵² surface energy scales with particle diameter (D) as:

$$\Delta S_{TS-MS} = \frac{6(\gamma_{MS} - \gamma_{TS})}{D} \dots (4)$$

where the γ_{MS} and γ_{TS} terms represent the interfacial surface energies of thermodynamic and metastable configurations, respectively; $g_s = A_{TS}/A_{MS}$ is the ratio of the interfacial surface areas for the two polymorphs. As such, nanoscale dimensions favor stabilization of the cubic polymorph.

Recent work has illustrated that a metastable polymorph can be preferentially stabilized if the barrier to nucleation of a metastable polymorph is lower than that of the thermodynamic phase.^{53,54} The barrier to nucleation can be written as:

$$\Delta G_n \propto \frac{(\eta\chi)^3}{(-RT \ln \sigma)^2} \dots (5)$$

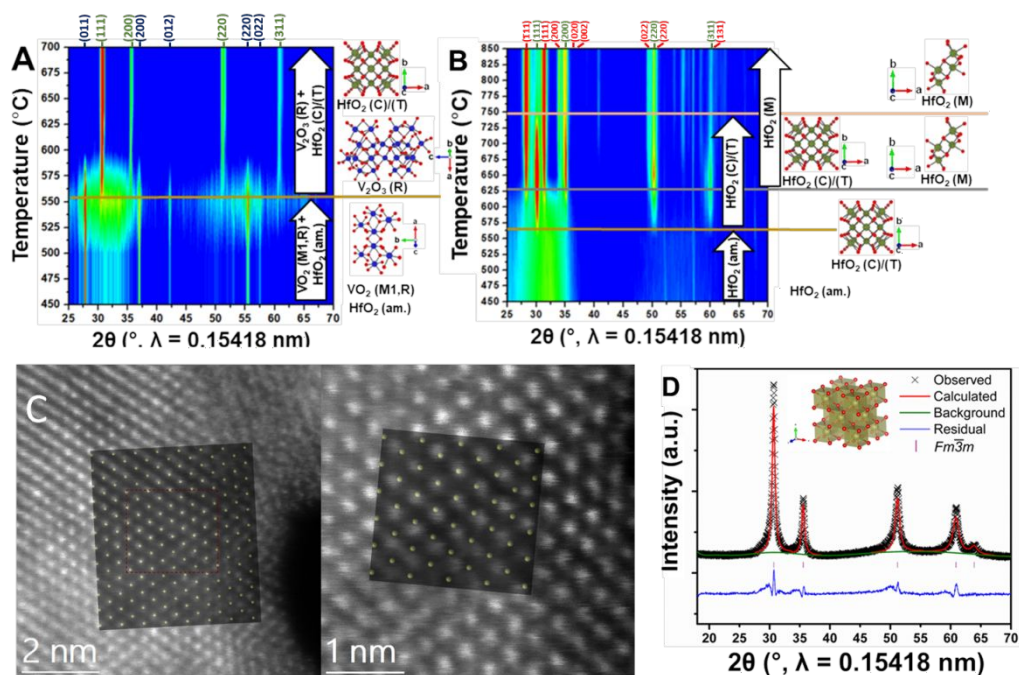


Figure 4: Temperature-dependent XRD patterns and structure refinement. **A)** Evolution of XRD patterns of VO₂@amorphous HfO₂ with increasing temperature. The (011) reflection of M1 VO₂ is attenuated as the (111) reflection for cubic hafnia begins to reach maximum intensity between 560 and 600°C. Crystal structures of the phases that are predominant within each temperature range are illustrated alongside the intensity map. **B)** Evolution of the powder XRD pattern in a control experiment omitting the VO₂ nanowires. Initially stabilized tetragonal/cubic HfO₂ domains disappear rapidly with sintering; the thermodynamically stable monoclinic phase of HfO₂ emerges as the dominant species. **C)** HRSTEM image of cubic HfO₂ along the [110] zone axis. The superimposed olive spheres are Hf atomic column positions in the [110] zone as predicted using CrystalMaker software. **D)** Observed XRD pattern (black crosses) plotted along with a refinement to cubic HfO₂. The simulated XRD pattern is displayed in red, background in green, and residual curve in blue; 2 θ positions of reflections are marked as purple ticks. The structure refines to cubic HfO₂ crystallized in the Fm $\bar{3}$ m space group (see Table S1 for refinement metrics).

where $\eta\chi$ is the surface energy (equivalent to S), σ represents the supersaturation, and thus $-RT\ln\sigma$ is the thermodynamic driving force for crystallization.^{53,54} If the surface energy of the metastable phase is lower, it can still be preferentially crystallized despite having a lower thermodynamic driving force for crystallization. The rhombohedral V₂O₃ core essentially selects for the preferential formation of cubic HfO₂ as compared to other HfO₂ polymorphs owing to the available epitaxial relationship (as well as the influence of vanadium incorporation). In other words, the coherent low-energy interface accessible between cubic-HfO₂ and rhombohedral V₂O₃ (but not with monoclinic HfO₂) facilitates selective crystallization of the former polymorph by depressing the nucleation barrier. Interestingly, while the epitaxial relationship likely underpins nucleation of cubic HfO₂, the lattice mismatch is sufficiently large such as to bring about strain-induced delamination of the V₂O₃ core from the HfO₂ shell and this mismatch is further evidenced in the small crystallite size of the stabilized domains (Figs. 3B and S5). Indeed, the crystallite size of cubic-HfO₂ is 8.4±1.4 nm, which suggests that extended coherent interfaces are not stabilized within this system.

The stabilization of free-standing cubic hafnia thereby provides access to a metastable kinetically trapped polymorph that is otherwise only accessible at temperatures above 2600°C. The cubic HfO₂ remains stable for over 12 months without transforming to metastable tetragonal or thermodynamically stable monoclinic polymorphs.

Synthesis of Negative Thermal Expansion HfV₂O₇: Conventional

(until a temperature of 150°C), followed by a subsequent increase to higher 2θ values up to 700°C. The initial increase and subsequent decrease of interplanar lattice separation with increasing temperature is indicative of the straightening of VO₃—O—VO₃ bonds and the subsequent transverse, volume-reducing oscillations of said bonds.^{31,32,34} The negative thermal expansion behavior is observed to be entirely reversible in the cooling panels of **Figure 7**.^{31,32,34}

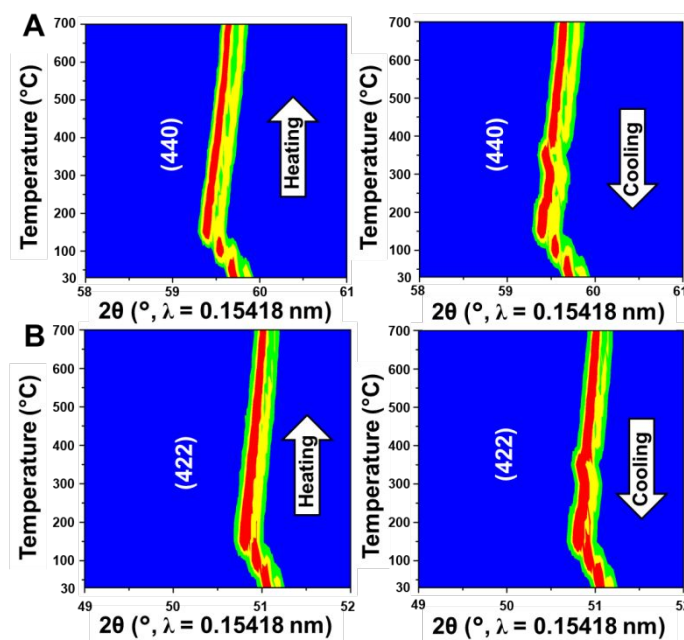
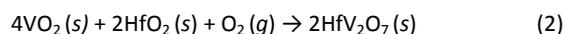


Figure 7. A) In situ temperature-variant powder XRD of HfV₂O₇ illustrating NTE behavior. Intensity modulation plots for A) (440) and B) (422) reflections of HfV₂O₇ plotted as a function of temperature. Shifts to lower and higher 2θ represent lattice expansion and compression, respectively. The right panels indicate the entirely reversible alteration of lattice constants upon cooling.

routes to the synthesis of HfV₂O₇ employ the grinding and sintering at 700°C of hafnium oxalic acid and ammonium oxodioxalato-vanadium *n*H₂O complexes in precise stoichiometric amounts.³² Other methods require copious amounts of organic solvents.⁴³ Here we demonstrate that annealing VO₂@amorphous-HfO₂ core-shell nanowires under static air instead of Ar yields HfV₂O₇ by dint of an interdiffusion reaction (albeit without preservation of the nanowire morphology) as per:



The reaction is strongly enthalpically favored and entropically disfavored. As such, a lower reaction temperature is imperative to facilitate high reaction yields but requires mitigating kinetic impediments to mixing of the precursors. The core-shell positioning of precursors outlined here allows for facile interdiffusion at relatively low temperatures enabling high conversion yields. **Figure 6** shows SEM and TEM images and an XRD pattern indicating the synthesis of HfV₂O₇. The core-shell structuring of precursors thus enables a facile low-temperature route for the stabilization of HfV₂O₇, which is an isotropic negative thermal expansion material.

In situ XRD data has been acquired to examine the evolution of products with increasing temperature. **Figure 7** shows variable-temperature powder X-ray diffraction data acquired for the HfV₂O₇ materials obtained by this approach.^{31,32,34} The evolution of two prominent reflections, (440) and (422), is shown in **Figure 7**. For both sets of reflections, a shift of 2θ to lower values is initially observed

Conclusions

In summary, we have demonstrated a facile low-temperature synthetic route for stabilizing the metastable cubic phase of HfO₂ under ambient conditions utilizing the epitaxial relationship between rhombohedral V₂O₃ (generated *in situ* from reduction of VO₂ as a result of oxygen diffusion) and cubic HfO₂.^{3,44} Oxygen diffusion proceeds from the VO₂ core to the amorphous HfO₂ shell owing to the more electropositive nature of the latter and the higher oxygen vacancy formation energy in crystalline HfO₂ as compared to amorphous HfO₂; the available epitaxial relationship along with incorporation of vanadium atoms reduces the barrier to nucleation of the cubic polymorph notwithstanding its metastable nature and allows for its preservation at elevated temperatures wherein sintering and grain growth strongly favors stabilization of the monoclinic phase.^{53,54} The formation of a low-energy coherent interface substantially reduces the barrier to nucleation of cubic HfO₂ domains despite its relatively lower thermodynamic driving force for crystallization as compared to the monoclinic phase. The epitaxial synthesis route thus serves as a valuable addition to strategies such as size reduction and introduction of twin domains used to stabilize metastable polymorphs of HfO₂.^{5,15}

The arrangement of VO₂ and HfO₂ in a core-shell structure further provides a direct solid-state synthetic route to cubic HfV₂O₇, a technologically important negative thermal expansion material.^{32,33,35} The core-shell positioning of precursors allows for

this entropically disfavored reaction to be performed at low temperatures with excellent conversion. Variable-temperature powder XRD measurements show pronounced negative thermal expansion behavior in the range between 150 and 700°C.^{3,45} Future work will focus on experimentally determining the dielectric constant of this polymorph as well as exploring epitaxial relationships with the rich available repertoire of VO₂ polymorphs to stabilize other metastable variants of HfO₂.

Conflicts of interest

There are no conflicts to declare.

Acknowledgements

We gratefully acknowledge partial support from the National Science Foundation under NSF grants DMR 1809866, DMR 1455154 (BSG), and OIA 1355438 (MPT). J.L.A. acknowledges support from a NASA Space Technology Research Fellowship under grant number 80NSSC17K0182. MPT acknowledges support from NASA Kentucky under NASA award No: NNX15AK28A. The research was funded in part by award # A-1978-20190330 from the Welch Foundation. The TAMU Materials Characterization Facility (MCF) is acknowledged for work done with the SEM and the TAMU Microscopy Imaging Center (MIC) is acknowledged for work done with TEM. A portion of this research was conducted at the Center for Nanophase Materials Sciences, which is a DOE Office of Science User Facility.

References

- 1 A. Navrotsky, *ChemPhysChem*, 2011, **12**, 2207–2215.
- 2 A. J. Martinolich & J. R. Neilson, *Chem. Mater.*, 2017, **29**, 479–489.
- 3 A. Parija, G. R. Waetzig, J. L. Andrews, & S. Banerjee, *J. Phys. Chem. C*, 2018, **122**, 25709–25728.
- 4 W. Sun et al., *Sci. Adv.*, 2016, **2**, e1600225.
- 5 B. M. Hudak et al., *Nat. Commun.*, 2017, **8**, 15316.
- 6 A. Navrotsky, L. Mazeina & J. Majzlan, *Science (80-.)*, 2008, **319**, 1635.
- 7 L. R. De Jesus, J. L. Andrews, A. Parija & S. Banerjee, *ACS Energy Lett.*, 2018, **3**, 915–931.
- 8 A. E. Powell, J. M. Hodges & R. E. Schaak, *J. Am. Chem. Soc.*, 2016, **138**, 471–474.
- 9 R. E. Schaak & T. E. Mallouk, *Chem. Mater.*, 2002, **14**, 1455–1471.
- 10 E. Bianco et al., *ACS Nano*, 2013, **7**, 4414–4421.
- 11 N. D. Cultrara et al., *Chem. Mater.*, 2018, **30**, 1335–1343.
- 12 R. C. DeVries, *Ann. Rev. Mater. Sci.*, 1987, **17**, 161.
- 13 J. C. Angus & C. C. Hayman, *Annu. Rev. Mater. Sci.*, 1988, **241**, 913–921.
- 14 R. C. Garvie, *J. Phys. Chem.*, 1965, **69**, 1238–1243.
- 15 G. R. Waetzig et al., *Chem. Sci.*, 2016, **7**, 4930–4939.
- 16 C. Garvie, *J. Phys. Chem.*, 1965, **69**, 1238–1243.
- 17 J. Chevalier, L. Gremillard, D. R. Clarke & D. R. Clarke, *J. Am. Ceram. Soc.*, 2009, **92**, 1901–1920.
- 18 J. Tang et al., *Adv. Funct. Mater.*, 2005, **15**, 1595–1602.
- 19 J. Joo et al., *J. Am. Chem. Soc.*, 2003, **125**, 6553–6557.
- 20 J. Tang et al., *Chem. Mater.*, 2004, **16**, 1336–1342.
- 21 D. Shin, R. Arróyave & Z. K. Liu, *Calphad Comput. Coupling Phase Diagrams Thermochem.*, 2006, **30**, 375–386.
- 22 J. Wang, H. P. Li & R. Stevens, *J. Mater. Sci.*, 1992, **27**, 5397–5430.
- 23 X. Luo, W. Zhou, S. V. Ushakov, A. Navrotsky & A. A. Demkov, *Phys. Rev. B - Condens. Matter Mater. Phys.*, 2009, **80**, 134119.
- 24 X. Zhao & D. Vanderbilt, *Phys. Rev. B*, 2002, **65**, 233106.
- 25 S. W. Depner, N. D. Cultrara, K. E. Farley, Y. Qin & S. Banerjee, *ACS Nano*, 2014, **8**, 4678–4688.
- 26 B. Zhou, H. Shi, X. D. Zhang, Q. Su & Z. Y. Jiang, *J. Phys. D: Appl. Phys.*, 2014, **47**, 115502.
- 27 T. S. Böske, J. Müller, D. Bräuhäus, U. Schröder & U. Böttger, *Appl. Phys. Lett.*, 2011, **99**, 102903.
- 28 R. Batra, T. D. Huan, G. A. Rossetti & R. Ramprasad, *Chem. Mater.*, 2017, **29**, 9102–9109.
- 29 T. V. Perevalov et al., *J. Appl. Phys.*, 2007, **101**, 053704.
- 30 W. He, L. Zhang, D. S. H. Chan & B. J. Cho, *IEEE Electron Device Lett.*, 2009, **30**, 623–625.
- 31 C. Turquat, C. Leroux, M. Roubin & G. Nihoul, *Solid State Sci*, 1999, **1**, 3–13.
- 32 C. Turquat, *Eur. Phys. J. Appl. Phys.*, 2000, **10**, 15–27.
- 33 J. S. O. Evans, *J. Chem. Soc.*, 1999, **Dalt. Trans.**, 3317–3326. doi:10.1039/A904297K
- 34 R. C. Buchanan & G. W. Wolter, *J. Electrochem. Soc.*, 1983, **130**, 1905.
- 35 V. Korthuis et al., *Chem. Mater.*, 1995, **7**, 412–417.
- 36 N. A. Fleer et al., *ACS Appl. Mater. Interfaces*, 2017, **9**, 38887–38900.
- 37 N. A. Fleer et al., *ACS Omega*, 2018, **3**, 14280–14293.
- 38 T. E. G. Alivio et al., *Chem. Mater*, 2017, **29**, 5401–5412.
- 39 X. Li, W. Cai, L. Colombo & R. S. Ruoff, *Nano Lett.*, 2009, **9**, 4268–72.
- 40 J. Zhu et al., *ACS Appl. Mater. Interfaces*, 2015, **7**, 27796–27803.
- 41 D. Rai, A. Kitamura, K. M. Rosso, T. Sasaki & T. Kobayashi, *Radiochim. Acta*, 2016, **104**, 583–592.
- 42 S. V. Ushakov, C. E. Brown & A. Navrotsky, *J. Mater. Res.*, 2004, **19**, 693–696.
- 43 T. Hisashige, T. Yamaguchi, T. Tsuji & Y. Yamamura, *J. Ceram. Soc. Japan*, 2006, **114**, 607–611.
- 44 E. J. Braham, J. L. Andrews, T. E. G. Alivio, N. A. Fleer & S. Banerjee, *Phys. Status Solidi Appl. Mater. Sci.*, 2018, **215**, 1–9.
- 45 P. M. Marley, G. A. Horrocks, K. E. Pelcher & S. Banerjee, *Chem. Commun.*, 2015, **51**, 5181–5198.
- 46 Y. Li, S. Ji, Y. Gao, H. Luo & M. Kanehira, *Sci. Rep.*, 2013, **3**, 1370.
- 47 K. E. Pelcher, M. R. Crawley & S. Banerjee, *Mater. Res. Express*, 2014, **1**, 035014.
- 48 K. Post & R. G. Robins, *Electrochim. Acta*, 1976, **21**, 401–405
- 49 N. Capron, *Appl. Phys. Lett.*, 2007, **91**, 192905
- 50 T. J. Chen & C. L. Kuo, *Microelectronics Reliability*, 2014, **54.6-7**, 1119–1124.
- 51 F. F. Lange, *J. Mater. Sci.*, 1982, **17.1**, 225–234.
- 52 R. Batra, H. D. Tran, & R. Ramprasad, *Applied Physics Letters*, 2016, **108(17)**, 172902.
- 53 B. R. Chen et al., *Nat. Commun.*, 2018, **9**, 2553.
- 54 W. Sun, D. A. Kitchaev, D. Kramer & G. Ceder, *Nat. Commun.*, 2019, **10**, 1–9.